



## Research papers

## Lithium-ion battery anomaly detection with variational autoencoder based on feature representation learning

Wenbin Li<sup>1</sup>\*, Yue Yang<sup>1</sup>, Stefan Pischinger

Chair of Thermodynamics of Mobile Energy Conversion Systems, RWTH Aachen University, Forckenbeckstraße 4, Aachen, 52074, Germany



## ARTICLE INFO

## Keywords:

Lithium-ion battery  
Anomaly detection  
Variational autoencoder  
Gaussian mixture distribution  
Feature representation learning

## ABSTRACT

Battery failure is an increasingly critical issue in lithium-ion battery applications, primarily arising from manufacturing defects and operational abuse. Non-invasive battery anomaly detection based on monitoring data is of significant importance as disassembling a battery pack is impractical. A fault diagnosis approach employing Gaussian Mixture Model and Variational Autoencoder is proposed to effectively extract anomalous features from voltage, temperature, current, and State of Charge. The latent features are utilized for binary and multi-categories anomaly diagnosis through clustering and Random Forest, respectively, including Internal Short Circuit, overcharge, and over-temperature scenarios. The cluster compactness of latent variable distribution is improved by incorporating Maximum Mean Discrepancy into the training loss. The model is validated with both simulation and real battery data, which yields well-separated latent features and outstanding performance with a total accuracy of 98 % for binary classification task. A total accuracy of 99 % is achieved for multi-label classification using self-supervised learning with 15 % fault data and 5% contamination in training set.

## 1. Introduction

With an increasing proportion of electrification in transportation and the wide spread of distributed energy storage, Lithium-Ion Battery (LIB) has received significant attention for its excellent power performance and high energy density in vehicle application and stationary energy storage system [1,2]. However, defective or inoperative batteries are unavoidable due to the massive manufacturing of LIB with multiple procedures and multi-materials involved [3], e.g., metal foreign matter contamination which may further cause ISC [4,5]. In addition, thermal, electrical, and mechanical abuse during usage can also cause cell abnormalities [3,6]. The abnormal cells show inconsistency in comparison to the others in the battery pack, which decreases the power performance, available energy, and even leads to serious accidents, such as ISC and thermal runaway [7].

As disassembling a battery pack is infeasible, non-invasive anomaly detection comes to one common solution for battery fault diagnosis [8]. To this end, cell inconsistency [9] is proposed for anomaly detection, which evaluates its deviation from overall cell performance based on external sensor signals, including voltage, current, and temperature. Existing approaches can be categorized into model-based methods, signal-based methods, and data-driven methods [9,10].

## 1.1. Model-based algorithms

Model-based algorithms typically incorporate a battery model, primarily an electrochemical model or an Equivalent Circuit Model (ECM). Cell anomalies are identified according to the deviation in estimated model parameters and internal states from a predefined threshold [11]. The ISC is studied by connecting an ISC resistor in parallel to the cell in [12,13]. The equivalent ISC resistance is estimated through balancing capacity in [12] and compared with a threshold of 100  $\Omega$  for anomaly detection, while the leakage current derived from Area under Curve (AUC) of the Incremental Capacity (IC) curves is used in [13]. However, the cell-level balancing capacity in [12] is difficult to obtain in practice, particularly in systems employing passive balancing without balancing current measurement or module-level active balancing. The IC curve in [13] is obtained at a constant low C-rate, which is impractical due to excessively long charging duration. In addition to ISC, the accelerated aging and lithium plating can be identified through other parameters in electrochemical mode such as capacity and the exchange current of lithium stripping according to [14]. The cell current is treated as an internal state instead of SOC in [15] to detect current measurement fault through comparing the estimated current against the measured signal.

Model-based algorithms embed fault mechanisms into the battery model and parameterize either the model or the anomaly components

\* Corresponding author.

E-mail address: [li\\_w@tme.rwth-aachen.de](mailto:li_w@tme.rwth-aachen.de) (W. Li).

inside, which require accurate modeling, detailed fault mechanisms, and significant computational consumption.

### 1.2. Signal-based algorithms

Signal-based methods assess battery disorder and inconsistency through signal decomposition, entropy features, and statistical features from raw measurement data [16–18]. In [16], wavelet transformation is employed to decompose voltage signals into frequency-band components, where abnormal cells presenting distinct frequency distributions are identified by density-based clustering algorithm. In [17], the authors calculate Shannon entropy and Sample entropy within sliding windows, and determine abnormal cells by comparing the individual entropy against the average. Statistical features are derived in [18] from the eigenvalues of the voltage covariance matrix using sliding windows. Outliers beyond a certain threshold are considered fault cells.

Instead of studying fault mechanisms in model-based algorithms, signal-based algorithms focus on feature extraction during pre-processing phase and perform classification based on its distributional and statistical characteristics. However, pre-processing requires significant computational sources, and fault determination based on machine learning models shows optimized performance compared to pure signal-based methods [19,20].

### 1.3. Data-driven algorithms

Conventional data-driven algorithms capture anomalous information and provide a logistical mapping between input data and the fault labels using supervised learning. In [21], Support Vector Machine (SVM) is proposed for anomaly detection. The anomalous features in the frequency domain are extracted from the voltage time series data via discrete cosine transform as the input of the SVM. In [22], frequency variation pattern is derived from cell voltage data via wavelet transform as the input of subsequent Random Forest (RF) for fault detection. The conventional machine learning methods require accurate fault labels for supervised learning which are difficult to obtain. Manual feature extraction is also required during data pre-processing.

To this end, unsupervised and semi-supervised methods that leverage deep learning generative models have gained increasing popularity for anomaly detection, where small labeled dataset is required and the feature extraction is embedded in deep learning models. The reconstruction residual between input and output is utilized in [23,24] for binary fault diagnosis. In [23], the VAE model is proposed for anomaly detection based on reconstruction residual. The VAE is trained on normal data to reconstruct the cell voltage under given charging profiles, and the adversarial training is used to optimize its robustness. The reconstructed voltage of the abnormal cells differs from the measured voltage, and the thermal runaway anomaly is determined according to the deviation by a certain threshold. The latent variables in VAE follow the standard Gaussian distribution with a single peak, which limits its ability to capture the multi-modal features. In addition, the proposed algorithm determines the anomaly based on a certain threshold of reconstruction deviation, which limits its application in multi-fault diagnosis.

In addition to the reconstruction residual, the feature representation learning in latent space is also widely employed for classification tasks, which presents distinguishable distributional discrepancy that enables both binary and multi-label classification. The residual based anomaly detection in [24] reveals no obvious distributional discrepancy in latent space between normal and abnormal cells in the TSNE visualization, indicating a need for a multi-modal feature distribution with optimized compactness within individual clusters.

Unlike the conventional VAE assuming a single Gaussian prior distribution, GMM-VAE, namely a VAE embedded with GMM, is proposed in this work for fault cell detection based on latent feature representation learning. The proposed GMM-VAE employs multi-peak GMM as

the prior to extract multi-modal fault characteristics from the input data. In addition to real cell data, ISC simulation using SPMe with various ISC resistance is used for multi-label case, presenting ISC with different severities. To avoid the collapse of GMM prior distribution, the information entropy is introduced into the weight of the individual Gaussian component as a regularization term.

This work focuses on applying feature representation learning to both binary and multi-label anomaly diagnosis. The main contributions are summarized as follows:

- Unsupervised learning is implemented for binary fault diagnosis using only normal cell data augmented with white noise. The latent features of normal cells are clustered through Density-Based Spatial Clustering of Applications with Noise (DBSCAN), and the binary anomaly detection is achieved based on the Euclidean distance to the cluster centroids.
- Self-supervised learning is implemented for multi-label classification task in which the ISC cells are divided into various ISC severities by ISC resistance. 15% of ISC data are used to train the subsequent RF classifier to distinguish ISC severity according to the latent variables of GMM-VAE.
- GMM is used as the prior distribution in the proposed VAE. The information entropy is introduced as a regularization term to the weight of individual Gaussian component in case the GMM collapses to single Gaussian distribution.
- The MMD loss is applied to the latent space to improve the cluster compactness. A distinguishable and well-separated feature distribution is obtained for both binary and multi-label classification tasks.
- The proposed model is evaluated with ISC simulation data with different ISC resistance ranging from 20 to 200  $\Omega$  using SPMe. In addition, an open-source fault battery dataset is used for further validation on real cell data.

The remainder of this article is structured as follows. The architecture of the GMM-VAE is introduced in Section 2. Section 3 explains the simulation and battery data used in this work, together with the results of data pre-processing. The validation results are presented and analyzed in Section 4. Section 5 evaluates the number of Gaussian components in GMM-VAE and the kernel number used in mk-MMD loss. Section 6 presents the main conclusions.

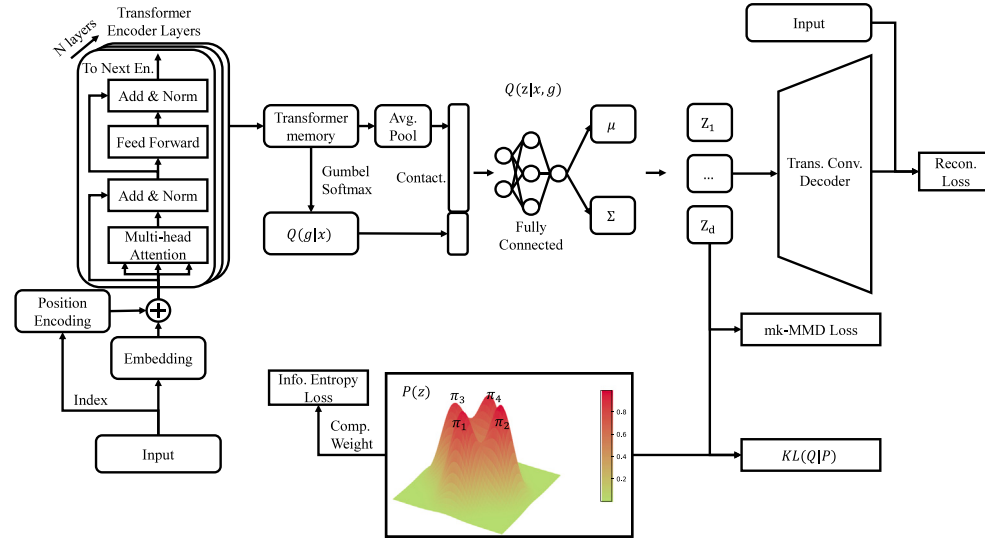
## 2. Proposed framework

Fig. 1(a) illustrates the architecture of the proposed GMM-VAE model built with encoder–decoder structure. The encoder consists of stacked Transformers with multi-head attention to extract anomalous features in latent space from the input sequence, while the decoder employs a transpose Convolutional Neural Network (CNN) to reconstruct the voltage and temperature signals based on the latent variables. The encoder's output is passed through an average pooling layer and projected to the mean and covariance values through Fully Connected (FC) layers, which are used to sample the latent features in the latent space.

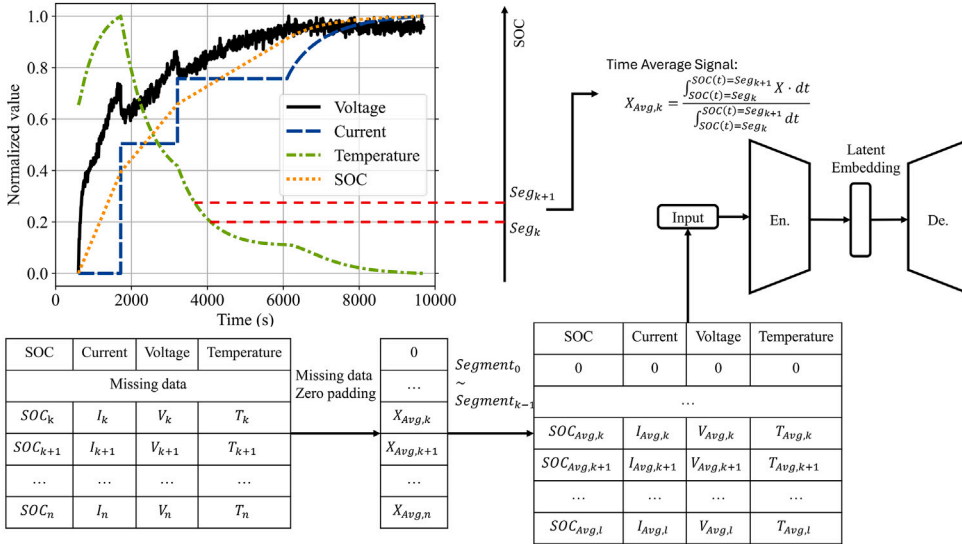
The Charging data are used as input, considering that the commonly used Multi-stage Constant Current (MCC) profile in real application is more stable than driving profiles. Furthermore, the time-averaged signals derived within fixed SOC segments according to Eq. (1) and Fig. 1(b) are used instead of the original time series data due to their varying data length.

$$X_{Avg,k} = \frac{\int_{SOC(t)=Seg_k}^{SOC(t)=Seg_{k+1}} X(t) \cdot dt}{\int_{SOC(t)=Seg_k}^{SOC(t)=Seg_{k+1}} dt} \quad (1)$$

The  $X$  in Eq. (1) stands for SOC, current, voltage, or temperature signals in Fig. 1(b),  $Seg_k$  stands for the  $k$ th SOC segment. By dividing the total SOC range into equal segments by 1%, the maximum input size is fixed



(a)



(b)

Fig. 1. The proposed GMM-VAE model for battery anomaly detection. (a) GMM-VAE model architecture; (b) Data pre-process.

to 100. Considering the varying input length due to different starting SOC, the missing data in the corresponding segments are processed with masking mechanism with zero padding as illustrated in Fig. 1(b). In this way, the model can adapt to varying input length.

In contrast to the conventional VAE which assumes a standard Gaussian prior, the proposed GMM-VAE in Fig. 1(a) utilizes the Gaussian Mixture Model with multiple peaks in Eq. (2) to learn multi-modal fault characteristics in the latent space.

$$\begin{aligned}
 P(z) &= \sum_{i=1}^k \pi_i \cdot N(\mu_i, \sigma_i) \\
 P(z|g, x) &= N(\mu_g, \sigma_g) \\
 P(g) &= Mult(\pi_1, \dots, \pi_k) \\
 Q(z|g, x) &= N(\mu(x), \sigma(x))
 \end{aligned} \tag{2}$$

In Eq. (2),  $g$  is an auxiliary variable which follows multi-category distribution, indicating to which modal the input belongs.  $\pi$ ,  $\mu$  and  $\sigma$  stand for the weight, mean value, and covariance of each Gaussian component, which are also trainable variables.

### 2.1. Variational autoencoder

The VAE assumes that the input data  $\vec{X} = \vec{x}_1, \dots, \vec{x}_N$  can be represented through a series of latent variables  $\vec{Z} = \vec{z}_1, \dots, \vec{z}_M$ . Therefore, the encoder suppresses the time series data into feature representation with fewer dimensions in the latent space ( $N > M$ ). The decoder reconstructs the input data based on latent variables. Since the real distribution of latent variables  $P(z|x)$  is unreachable, VAE introduces a trainable  $Q(z|x)$  as an approximation. The discrepancy between the real and approximated distribution is evaluated through the Kullback-Leibler Divergence (KLD) loss according to the following formula:

$$\begin{aligned}
 KLD(Q(z|x) \parallel P(z|x)) &= -E_Q[\log P(x|z)] + E_Q[\log P(x)] + \\
 &E_Q[\log Q(z|x) - \log P(z)]
 \end{aligned} \tag{3}$$

where,  $z, x$  stand for the latent variables and input data,  $E_Q$  stands for the expectation on  $Q(z|x)$ ,  $P(x)$  is the distribution of input data which is a constant term to maximize in Eq. (4).

Considering that the first KLD term in Eq. (4) is always positive, it is equivalent to maximizing the Evidence Lower Bound (ELBO) on the right side.

$$\log P(x) = \underbrace{KLD(Q(z|x) \| P(z|x)) + E_Q[\log P(x|z)] - KLD(Q(z|x) \| P(z))}_{\text{Reconstruction}} \quad (4)$$

$$\underbrace{\hspace{10em}}_{\text{ELBO}}$$

The first term in ELBO is the expectation of reconstructed data on  $Q(z|x)$  which is considered as the reconstruction loss and evaluated by the Mean Square Error (MSE) loss between the output and the input of the VAE. The second term is KLD loss that evaluates the distribution discrepancy between  $Q$  and  $P$ .

Considering that the input data consist of latent variables with multiple modals, the GMM with  $k$  components in Eq. (2) is used as the prior distribution. The ELBO is modified to Eq. (5) [25,26]:

$$\begin{aligned} ELBO &= E_Q[\log P(x|z, g)] - E_Q[\log Q(z, g|x) - \log P(z, g)] \\ &= E_Q[\log P(x|z, g)] - E_g[KLD(Q(z|x, g) \| P(z|g))] - \\ &KLD(Q(g|x) \| P(g)) \end{aligned} \quad (5)$$

where  $E_g$  stands for the expectation on  $Q(g|x)$ .  $P(z|g)$  and  $Q(z|x, g)$  are prior and posterior distribution of latent variables  $z$  of component  $g$ , which are assumed to follow Gaussian distribution.

## 2.2. Training process

As illustrated in Fig. 1(a), the total training loss in Eq. (6) consists of reconstruction loss, KLD loss, information entropy, and MMD.

$$\begin{aligned} L(x) &= L_{Recon.} + \beta \cdot L_{KL} + \gamma \cdot L_{Info.} + L_{mk-MMD} \\ L_{Recon.} &= \frac{1}{N} \cdot \sum_{i=1}^N (x_i - y_i)^2 \\ L_{Info.} &= -\sum_{i=1}^k \pi_i \cdot \log \pi_i \end{aligned} \quad (6)$$

The  $L_{Recon.} + \beta \cdot L_{KL}$  is the ELBO in Eq. (5),  $x$  and  $y$  stand for the input and output,  $\pi$  is the weight of Gaussian component,  $\beta$  and  $\gamma$  stand for the weights of  $L_{KL}$  and  $L_{Info.}$  which are adjusted using the sigmoid annealing algorithm in Eq. (7),

$$\lambda(N) = \lambda_{max} \cdot \frac{1}{1 + \exp(\frac{-k(N-N_0)}{N_0})} \quad (7)$$

where  $N$  stands for the training epoch,  $\lambda_{max}$  stands for the final weight,  $k$  controls the steepness, and  $N_0$  is the midpoint of annealing. Considering that the prior distribution is randomly initialized and is not well built in the early training stage, the annealing algorithm gradually and smoothly increases the weight of  $L_{Info.}$  and  $L_{KL}$ . This avoids over-regularization, preventing the encoder from being constrained by an immature prior, allowing the model to focus on learning robust reconstructions and stable representations.

According to the grid search results in Table S1 and S2, the maximum weights of  $L_{Info.}$  and  $L_{KL}$  are set to 0.2 in this work, the steepness  $k = 0.01$  is used to control the speed of adjustment, and the midpoint  $N_0$  takes 300 training epochs.

The information entropy  $L_{Info.}$  in Eq. (6) is applied to the weights of individual Gaussian components  $\pi$  as a regularization term to avoid GMM collapsing into single Gaussian distribution. The amount of Gaussian component  $k$  used in this work is 6.

The  $L_{mk-MMD}$  in Eq. (6) stands for the MMD loss with multiple Gaussian kernels as formulated in Eq. (8).  $k_p$  is the Gaussian kernel and  $\sigma_p^2$  stands for the variance of Gaussian kernel which is updated from the

total variance of the input latent feature  $x$ .

$$\begin{aligned} L_{MMD,p} &= \frac{1}{m \cdot (m-1)} \sum_i^m \sum_{j \neq i}^m k_p(x_{s,i}, x_{s,j}) \\ &- \frac{2}{m \cdot n} \sum_i^m \sum_j^n k_p(x_{s,i}, x_{t,j}) \\ &+ \frac{1}{n \cdot (n-1)} \sum_i^n \sum_{j \neq i}^n k_p(x_{t,i}, x_{t,j}) \end{aligned} \quad (8)$$

$$k_p(x_s, x_t) = \exp\left(-\frac{\|x_i - x_j\|_2^2}{2 \cdot \sigma_p^2}\right)$$

$$L_{mk-MMD} = \sum_{p=1}^N L_{MMD,p}$$

$$\sigma_p^2 = \frac{\sum_i^{m+n} \sum_{j \neq i}^{m+n} (x_i - x_j)^2}{(m+n) \cdot (m+n-1)} \cdot 2^{p-\frac{N+1}{2}}$$

The MMD loss minimizes the distribution discrepancy of feature representation to enhance cluster cohesion in the latent space. For unsupervised training, the calculation of MMD loss is iterated over all pairwise combinations to achieve global minimization on normal cell data. In the self-supervised training case, input data are partitioned according to labels to calculate MMD loss independently within each individual group, so that features from the same category are tightly clustered and separable from the others.

In comparison to the MMD with fixed kernel facing early collapse as the feature discrepancy converges, the multi-kernel MMD  $L_{mk-MMD}$  updates the bandwidth of each kernel through exponential scaling with a base of two based on the total variance at each training epoch. This dynamic adjustment prevents kernel from collapsing, maintains the sensitivity of the MMD loss and provides robust gradients. Considering the trade-off between complexity and performance, kernel number  $N$  is 5 in this work, which is discussed in Section 5 in detail.

## 2.3. Model configuration

Three approaches are compared in Section 4, including reconstruction residual approach based on conventional VAE, feature learning approaches based on autoencoder and the proposed GMM-VAE. The reconstruction loss and MMD loss converge after 500 training epochs without overfitting till up to 1000 training epochs according to the deviation between training loss and validation loss. As listed in Table 1, identical encoder memory footprints can be found because all three models share the same encoder and decoder structure. For the fault diagnosis, both GMM-VAE and autoencoder require only the encoder and the latent layer for deployment to obtain the latent features, whereas the reconstruction residual based methods need the full model. A comparable inference time across three models can be found in Table 1 which is derived based on a personal computer (CPU Intel Core i7-13700k and GPU RTX 4080), including both the encoding and the decoding. The proposed method can be executed within 50 ms.

## 3. Dataset and experiment

An open-source dataset [27] from KIT using Nickel Manganese Cobalt (NMC) battery with a nominal capacity of 3 Ah is used for binary fault diagnosis. The dataset provides aging data measured by Battery Management System (BMS) based on cyclic, calendric, and driving profile, from the beginning to the end of life, considering the effects of the C-rate, the SOC range, and the temperature. In total, 55 cell channels raise fault indicators for overcharge, including overcharge capacity and over SOC, and over-temperature, which are labeled as abnormal cells in this work.

In addition, the SPMe from PyBamm [28] is utilized to generate cell data for multi-label anomaly detection through ISC simulation with various ISC severities. As illustrated in Fig. 2, ISC resistors  $R_{ISC}$  of

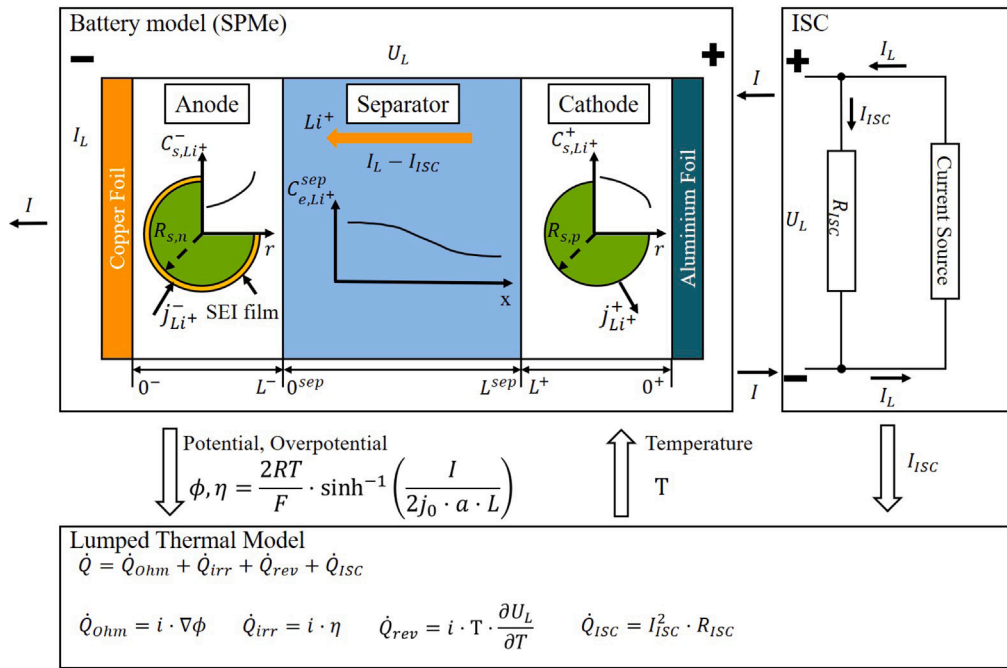


Fig. 2. The ISC model using SPMe.

Table 1

Detailed information regarding model configuration.

Framework	Network type	Memory size (kB)	Inference time (ms)
Autoencoder	Encoder: Transformer	812.75	41.66
	Latent layer: FC	111.00	
	Decoder: Transposed CNN	12.57	
GMM-VAE	Encoder: Transformer	812.75	41.69
	Latent layer: FC	124.56	
	Decoder: Transposed CNN	12.57	
VAE	Encoder: Transformer	812.75	43.25
	Latent layer: FC	15	
	Decoder: Transposed CNN	12.57	

200 Ω, 100 Ω, 50 Ω, 20 Ω are used in parallel external circuit to simulate an ISC current  $I_{ISC}$  ranging from 20 mA to 200 mA.

The SPMe employs parameters of a commercial cylindrical 21700 cell (LGM50) from [29], with NMC 811 cathode, Graphite – SiO<sub>x</sub> composite anode, and a nominal capacity of 5 A h. The simulation consists of an AST using Constant Current (CC) charging and discharging profile for 2000 cycles at ambient temperature 20 °C, and a characterization test with MCC, Constant Voltage (CV) charging, and CC discharging profiles at every 100 aging cycles, from which the charging data are used for fault diagnosis. The initial SOC of the MCC-CV charging stage is randomly selected from 5%~10%, and the C-rate at each CC stage of MCC profile is randomly selected from the given range, considering the potential power limitation of the off-board charger. The detailed simulation setting can be found in Table 2.

The SPMe model in Fig. 2 assumes an identical current distribution in the electrode and incorporates the electrolyte dynamics based on the Single Particle Model. The governing equations of solid phase diffusion and electrolyte diffusion in positive electrode, separator, and negative electrode are formulated in Eqs. (9) and (10)[30]:

$$\frac{\partial C_{s,Li^+}}{t} = \frac{1}{r_s^2} \cdot \frac{\partial}{\partial r_s} (D_s \cdot r_s^2 \cdot \frac{\partial C_{s,Li^+}}{\partial r_s})$$

$$\frac{\partial C_{s,Li^+}}{t} \Big|_{(r_s=0)} = 0$$

$$\frac{\partial C_{s,Li^+}}{t} \Big|_{(r_s=R_s)} = \mp \frac{I}{F \cdot a \cdot L \pm}$$

(9)

Table 2

AST simulation overview.

Test	Profile	Comments
AST	Charge at 0.7 C until 4.2 V Discharge at 1.5 C until 2.8 V	Conduct 2000 aging cycles in total under 20 °C
Characterization	Charge: CC1: 1~2 C until 4.0 V CC2: 0.5~1 C until 4.1 V CC3: 0.1~0.5 C until 4.2 V CV: 4.2 V until 20 mA Discharge: 0.2 C until 2.8 V	Conduct at every 100 aging cycles with initial temperature at 20 °C. C-rate in CC charge stage is randomly selected from the given range.

$$\frac{\partial C_{e,Li^+}^{\pm}}{t} = \frac{\partial}{\partial x} \left( \frac{D_e^{\pm}}{e^{\pm}} \cdot \frac{\partial C_{e,Li^+}^{\pm}}{\partial x} \right) \mp \frac{1-t^{\pm}}{e^{\pm} \cdot F \cdot L^{\pm}} \cdot I$$

$$\frac{\partial C_{e,Li^+}^{sep}}{t} = \frac{\partial}{\partial x} \left( \frac{D_e^{sep}}{e^{sep}} \cdot \frac{\partial C_{e,Li^+}^{sep}}{\partial x} \right)$$

$$\frac{\partial C_{e,Li^+}}{t} \Big|_{x=0^{\pm}} = 0$$

$$D_e^- \cdot \frac{\partial C_{e,Li^+}^-}{\partial x} \Big|_{x=L^-} = D_e^{sep} \cdot \frac{\partial C_{e,Li^+}^{sep}}{\partial x} \Big|_{x=0^{sep}}$$

$$D_e^{sep} \cdot \frac{\partial C_{e,Li^+}^{sep}}{\partial x} \Big|_{x=L^{sep}} = D_e^+ \cdot \frac{\partial C_{e,Li^+}^+}{\partial x} \Big|_{x=L^+}$$

(10)

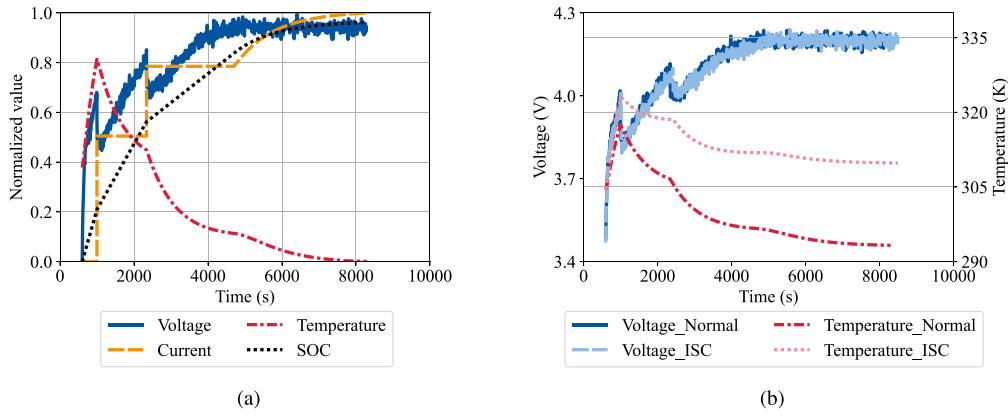


Fig. 3. The cell simulation data using SPMe. (a) Charging data of normal cell; (b) Voltage and temperature comparison between normal cell and ISC cell.

where,  $C_{s, Li^+}$ ,  $C_{e, Li^+}$ ,  $D_s$ , and  $D_e$  represent the concentration of lithium-ion and diffusion coefficients in solid and electrolyte phase,  $I$  stands for the cell current,  $F$  is the Faraday constant,  $a_s$  is the volume-specific surface area,  $t^+$  is the transference number of lithium-ion.

The relationship between external load current  $I_L$ , ISC leakage current  $I_{ISC}$  and cell current in Fig. 2 can be derived from Eq. (11):

$$\begin{aligned} I &= I_L - I_{ISC} \\ &= I_L - \frac{U_L}{R_{ISC}} \end{aligned} \quad (11)$$

## 4. Results and analysis

### 4.1. Sliding window average based on SOC segment

In total, 60 normal cells and 60 ISC cells with ISC resistance varying from 20 to 200  $\Omega$  are simulated by SPMe models. The simulation results under 3CC-CV charging profile are presented in Fig. 3(a). Because the minus current stands for charging, the Min-Max normalized value of the current signal increases from 0 to 1 as the charging current decreases to cut-off current in CV stage in Table 2. Cell voltage and temperature of one normal cell and one ISC cell with an ISC resistance of 20  $\Omega$  under the same charging profile are illustrated in Fig. 3(b). Due to the existence of ISC current, extra heat generation is observed in the ISC cell, resulting in a higher temperature increase compared to the normal cell. In addition, a delay in voltage increase is observed in the ISC cell in Fig. 3(b), indicating a corresponding delay in the SOC increase. The delay is attributed to the reduced effective charging current due to the leakage current  $I_{ISC}$  as depicted in Fig. 2, despite the same load current  $I_L$  applied to both cells in the external circuit.

Fig. 4 presents the cell voltage and temperature results processed by the sliding window algorithm in Eq. (1) based on SOC segment. The ISC cell reaches the CV stage later than the normal cell, leading to warping of the voltage curve in Fig. 4(a). The discrepancy arises due to the existence of leakage current in Eq. (11) in ISC cells, which reduces the real increase of SOC and postpones the charging phase. Furthermore, an additional temperature increase is observed in Fig. 4(b) for ISC cells. The leakage current generates extra heating power and causes an additional temperature increase.

Fig. 4(c) and(d) illustrate the sliding-window-averaged voltage and temperature for normal cells and abnormal cells undergoing over SOC and over temperature faults in KIT dataset. Due to a charging current control failure, the over SOC cell is subjected to high-current charging when it reaches the cut-off voltage. During the subsequent charging process, an abnormal voltage drop is observed while the charging current increases, indicating an internal defect in the over SOC cell. In Fig. 4(d), the over-temperature cell shows an abnormal temperature increase of 20 K compared to 3 K for the normal cell during charging.

### 4.2. Binary anomaly detection based on latent feature representation

Unsupervised training is first implemented for binary fault diagnosis with real cell data from KIT dataset [27], which provides fault data and labels for overcharge and over-temperature error during aging tests. As multiple fault indicators are raised during the test, only the binary fault diagnosis is validated in this section. Input data are processed as illustrated in Fig. 1(b) through sliding window average based on SOC segment in Eq. (1), including Voltage, temperature, and SOC from real BMS signals. The entire normal dataset is split into training, validation and testing sets according to a ratio of 0.5:0.2:0.3 randomly. All abnormal data are used in the testing dataset.

The reconstruction residual based approach is compared with the feature representation learning based approach using GMM-VAE with identical latent feature dimensions of 16 and six Gaussian components by evaluating their latent space distributions in Fig. 5(a) and (b) through TSNE dimension reduction. Although some latent features of abnormal cells are distinguishable from the normal cell in Fig. 5(a) while reconstruction loss and KLD loss are implemented for reconstruction residual based approach, a substantial portion of latent features remain overlapped. In contrast, a well-separated latent variables distribution can be observed between normal and abnormal cells in Fig. 5(b) while MMD loss is applied to the latent space for feature representation learning, indicating a superior performance in distinguishing latent features from normal cells and abnormal cells for feature representation learning based approach with MMD loss involved.

To quantify the distribution discrepancy for anomaly detection, the DBSCAN algorithm is employed to derive cluster centroids from the latent features of normal cells. The minimum Euclidean distance between the latent variables and cluster centroids serves as detection metric. The Euclidean distance metric is illustrated as a histogram in Fig. 5(c), where the x-axis is the MinMax-normalized Euclidean distance to the cluster centroids. A subtle overlap can be found between normal and abnormal cells for the distance deviation below 0.05. In contrast, a significant overlap can be found for the reconstruction deviation extending up to 0.2, which aligns with the TSNE visualization in Fig. 5(a) and (b).

The confusion matrix in Table 3 and Eq. (12) is one of the most commonly used metrics to evaluate the accuracy of a binary classifier, where True Positive Rate (TPR) and True Negative Rate (TNR) demonstrate the proportion of accurate prediction of positive and negative samples respectively. Since the summary of False Positive Rate (FPR) and TPR is one, only TPR is given here, which is the same case for False Negative Rate (FNR).

$$\begin{aligned} \text{TNR} &= \frac{\text{TN}}{\text{TN} + \text{FP}} \\ \text{TPR} &= \frac{\text{TP}}{\text{TP} + \text{FN}} \\ \text{Total accuracy} &= \frac{\text{TN} + \text{TP}}{\text{TN} + \text{FN} + \text{TP} + \text{FP}} \end{aligned} \quad (12)$$

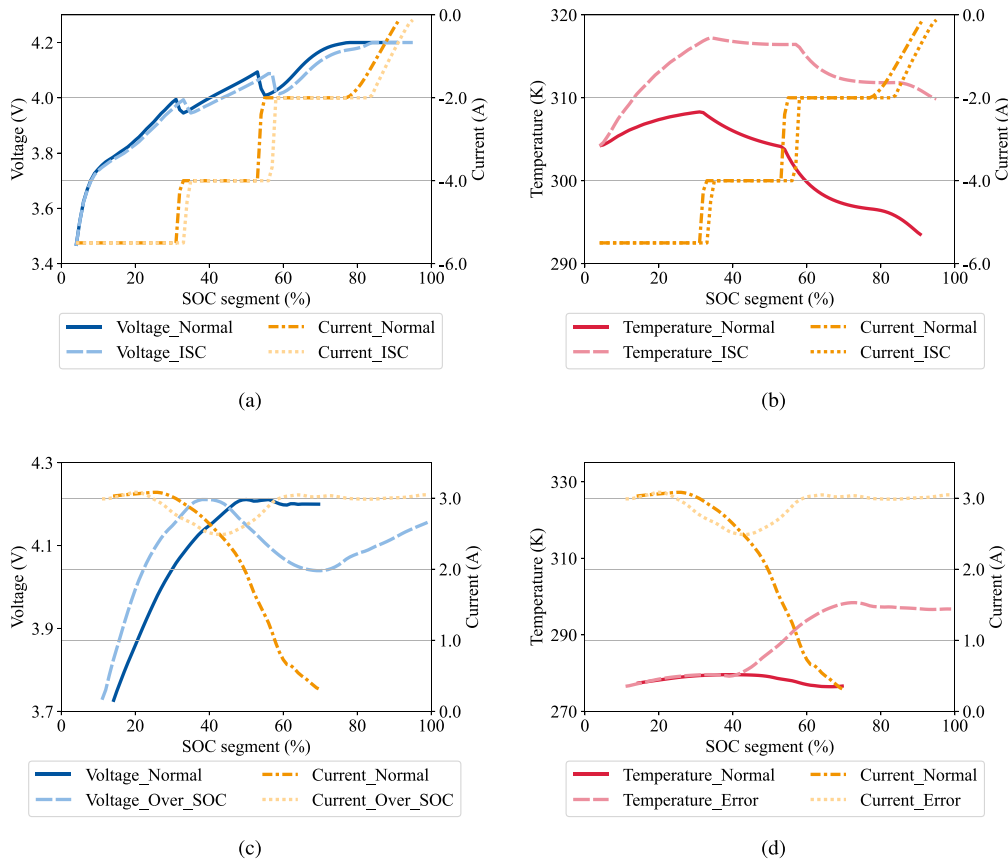


Fig. 4. Data after time averaging based on SOC segment. (a) PyBamm ISC voltage simulation; (b) PyBamm ISC temperature simulation; (c) KIT over SOC; (d) KIT temperature measure error.

Table 3  
Confusion matrix calculation.

		Prediction result	
		Negative	Positive
Real label	Negative	TN	FN
	Positive	FP	TP

The Receiver Operating Characteristic (ROC) in Fig. 5(d) demonstrates the trade-off between TPR and FPR across different thresholds. The AUC ranging between 0.5 and 1.0 quantifies the sensitivity of the binary classifier to the threshold, which demonstrates a stronger robustness to the threshold change as it approaches towards 1.0. The optimal threshold can be identified as the bending point on the ROC curve, which maximizes the vertical distance from the reference curve.

The ROC curve in Fig. 5(d) presents an AUC of 0.98 for positive sample identification using latent variables, which significantly outperforms the method based on reconstruction residual due to the overlapping distribution in the histogram in Fig. 5(c).

The confusion matrix in Table 4 demonstrates a superior performance over the reconstruction-based approaches using VAE and the generative model in [31] while using latent features from autoencoder and GMM-VAE. Similar accuracy can be achieved compared to the other supervised learning method in [32], while using unsupervised learning based on latent feature deviation.

The results present a TPR of 0.82 and a TNR of 0.97 for abnormal cell detection, as the latent features of autoencoder are used. The performance is improved to 0.98 when GMM-VAE is implemented for feature extraction, using a normalized deviation threshold of 0.05, which can be derived from the bending point of AUC curve in Fig. 5(d).

Table 4  
Confusion matrix for binary fault detection (KIT).

	Metric	Normal cell	Abnormal cell
VAE Reconstruction	TPR	0.59	0.71
	TNR	0.71	0.59
	Total accuracy	0.67	0.67
Gated Recurrent Unit [32]	TPR	/ <sup>a</sup>	0.92
	TNR	0.92	/
	Total accuracy	0.97	0.97
Generative model Reconstruction [31]	TPR	/	0.87
	TNR	0.87	/
	Total accuracy	/	/
Autoencoder + MMD	TPR	0.97	0.82
	TNR	0.82	0.97
	Total accuracy	0.89	0.89
GMM-VAE + MMD (proposed method)	TPR	0.98	0.98
	TNR	0.98	0.98
	Total accuracy	0.98	0.98

<sup>a</sup> /means data are not available in the reference work.

### 4.3. Anomaly detection based on ISC simulation

Binary anomaly detection is further validated on ISC simulation data with classification results summarized in Fig. 6 and Table 5. Consistent with the case in Section 4.2, the feature representation learning based approach exhibits a distinguishable divergency in latent space distribution between normal cells and abnormal cells in Fig. 6(b). In contrast, the reconstruction residual based method presents an obvious overlap in latent variables distribution in Fig. 6(a).

As illustrated by the ROC curve in Fig. 6(d), the feature representation learning methods (autoencoder and GMM-VAE) present superior robustness for binary fault diagnosis with AUC values of 0.97 and

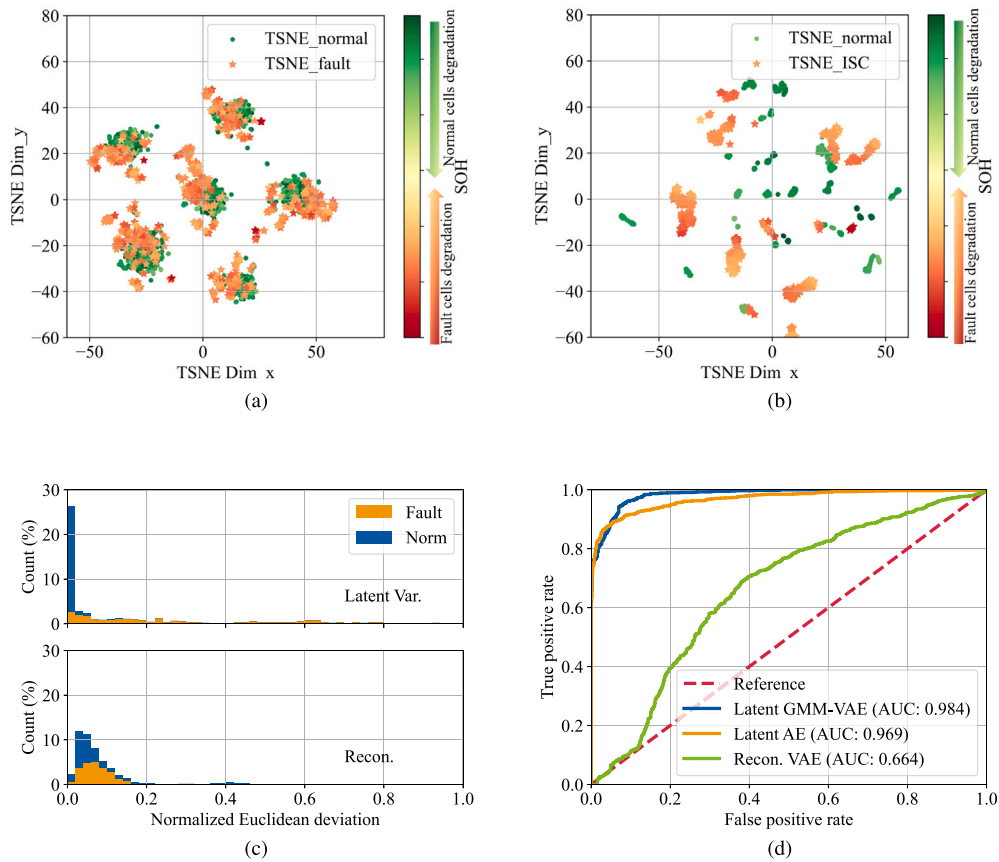


**Fig. 5.** Binary fault diagnosis using KIT dataset. (a) Reconstruction error distribution in TSNE view; (b) Latent variables distribution in TSNE view; (c) Histogram of relative deviation to cluster centroid and relative reconstruction residual; (d) ROC analysis of binary fault diagnosis.

0.98 compared to the AUC value of 0.81 for the reconstruction-based approach. A threshold of 0.04 is derived for the minimum normalized distance to the cluster centroids, by which the ISC cells can be differed from the normal cells.

As shown in Table 5, the ISC detection accuracy achieves a total accuracy of 0.95 for both normal and ISC cells as autoencoder with MMD loss is implemented, which improves to 0.98 when GMM-VAE is used. The proposed unsupervised method based on latent feature learning significantly outperforms the reconstruction residual based approaches using VAE. The prominent performance is consistent with the TSNE visualization and histogram in Fig. 6(b) and (c). In contrast, the significant overlap of reconstruction error distribution in Fig. 6(a) and (c) leads to a lower total accuracy of 0.73 for reconstruction residual based method.

Furthermore, this unsupervised approach also achieves a superior performance over the conventional supervised learning method using SVM in [33] and a comparable total accuracy in respect of the other supervised deep learning approach in [34] and model-based approach in [35].

In addition to the unsupervised fault diagnosis, a self-supervised multi-label classification is implemented that categorizes ISC cells into various levels of ISC severity based on the ISC resistance. The mk-MMD loss term in Eq. (6) is applied independently within each category during the training process. The total normal and ISC data are split into training, validation, and testing datasets according to a ratio of 0.5:0.2:0.3 randomly.

To comprehensively evaluate the performance under an unseen subtle leakage current during training, further simulation results with ISC resistance of 400, 600, 800 and 1000 $\Omega$  are included in the testing set. Additionally, 5% ISC data are added into the normal cell training

**Table 5**

Confusion matrix for binary ISC detection.

	Metric	Normal cell	ISC cell
VAE Reconstruction	TPR	0.75	0.71
	TNR	0.71	0.75
	Total accuracy	0.73	0.73
Model-based ISC estimation [35]	TPR	1.00	0.96
	TNR	0.96	1.00
	Total accuracy	0.97	0.97
Deep Multi-Layer Perception (MLP) [34]	TPR	1.00	<sup>a</sup>
	TNR	/	1.00
	Total accuracy	0.93~1.00	0.93~1.00
SVM [33]	TPR	/	/
	TNR	/	/
	Total accuracy	0.89	0.89
Autoencoder + MMD	TPR	0.97	0.92
	TNR	0.92	0.97
	Total accuracy	0.95	0.95
GMM-VAE + MMD (proposed method)	TPR	1.00	0.97
	TNR	0.97	1.00
	Total accuracy	0.98	0.98

<sup>a</sup> /means data are not available in the reference work.

set to evaluate the performance when training set is contaminated with unlabeled abnormal data.

The TSNE visualization in Fig. 7 illustrates the latent feature distribution of normal cells and abnormal cells with ISC resistance of 20, 50, 100, and 200 $\Omega$ . The latent features are compactly distributed within each individual cluster, representing a distinguishable and well-separated distribution.

Subsequently, latent features of a held-out category of subtle ISC cases are obtained through the pre-trained model mentioned above without further training to investigate its zero-shot capability to detect

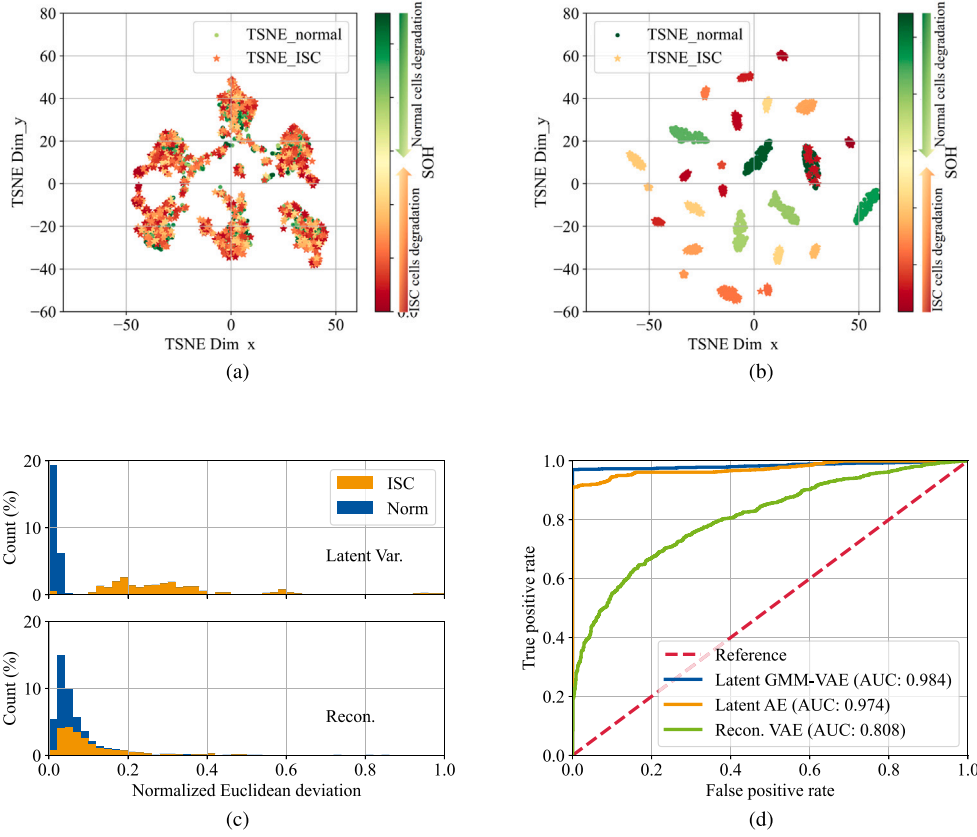


**Fig. 6.** Binary fault diagnosis using ISC simulation. (a) Reconstruction error distribution in TSNE view; (b) Latent variables distribution in TSNE view; (c) Histogram of relative deviation to cluster centroid and relative reconstruction residual; (d) ROC analysis of binary fault diagnosis.

unseen anomalies in the pre-training stage. A binary classifier based on RF with 10 trees and depth of 16 is trained to distinguish normal cells and ISC cells, including the ISC cases during training. Another multi-label RF classifier using the same configuration is trained to distinguish ISC cells with ISC resistance of 20, 50, 100, and 200Ω. The additional ISC cases are considered in the binary ISC cases because the MMD loss is not implemented with unlabeled data during the training process. Therefore, the latent feature of the other ISC cells cannot present a compact distribution as shown in Fig. 7. The classification results are summarized in Table 6 when 5%, 10%, 15% and 20% ISC data are used for training, respectively.

Both the binary and the multi-label classifiers present improved performance as the proportion of fault data in the training set increases. The TPR of binary classifier increases from 0.82 to 0.96 and 0.99 as the proportion of training fault data increases from 5% to over 15%, while the TPR of multi-label classifier increases from 0.4 to 0.96 and the total accuracy increases from 0.9 to 0.99.

Self-supervised learning with limited labeled abnormal data shows remarkable practice considering the difficulty of collecting and labeling fault data. Note that all 50% normal cell data for GMM-VAE training are used to train the RF, considering that normal cell data can be easily obtained compared to abnormal cell data. The increasing TPR and TNR indicate a lower misdiagnosis rate through the proposed approach.

### 5. Hyperparameter sensitivity analysis

The hyperparameter selection is discussed in this section, including the number of Gaussian components in the GMM prior and the number of Gaussian kernels in the k-MMD loss, taking the ISC case as an example.

**Table 6**

Confusion matrix for multi-label ISC detection.

	Metric	Latent feature learning (Trained with 5%/10%/15%/20% fault data)
Normal cell	TPR	1.00/1.00/1.00/1.00
	TNR	0.82/0.96/0.99/0.99
	Total accuracy	0.91/0.98/0.99/0.99
ISC cell (total)	TPR	0.82/0.96/0.99/0.99
	TNR	1.00/1.00/1.00/1.00
	Total accuracy	0.91/0.98/0.99/0.99
ISC 20Ω	TPR	0.40/0.96/0.96/0.96
	TNR	0.96/0.98/0.99/0.99
	Total accuracy	0.90/0.97/0.99/0.99
ISC 50Ω	TPR	0.68/0.86/0.99/0.99
	TNR	0.97/0.99/0.99/0.99
	Total accuracy	0.94/0.98/0.99/0.99
ISC 100Ω	TPR	0.99/0.99/0.99/0.99
	TNR	0.93/0.99/0.99/0.99
	Total accuracy	0.95/0.99/0.99/0.99
ISC 200Ω	TPR	0.79/0.98/0.99/0.99
	TNR	0.99/0.98/0.99/0.99
	Total accuracy	0.97/0.98/0.99/0.99

#### 5.1. Gaussian component evaluation using Bayesian information criterion

As mentioned at the end of Section 1, the GMM prior can fit the multi-modal distribution in the latent space to approximate the real latent distribution by using a weighted combination of multiple Gaussian components. The Bayesian Information Criterion (BIC) in Eq. (13) is used to evaluate the number of Gaussian components.  $\log(\hat{L})$  stands for the likelihood that the latent features fit the given GMM,  $P$  stands for the number of hyperparameters of GMM, including weights, mean

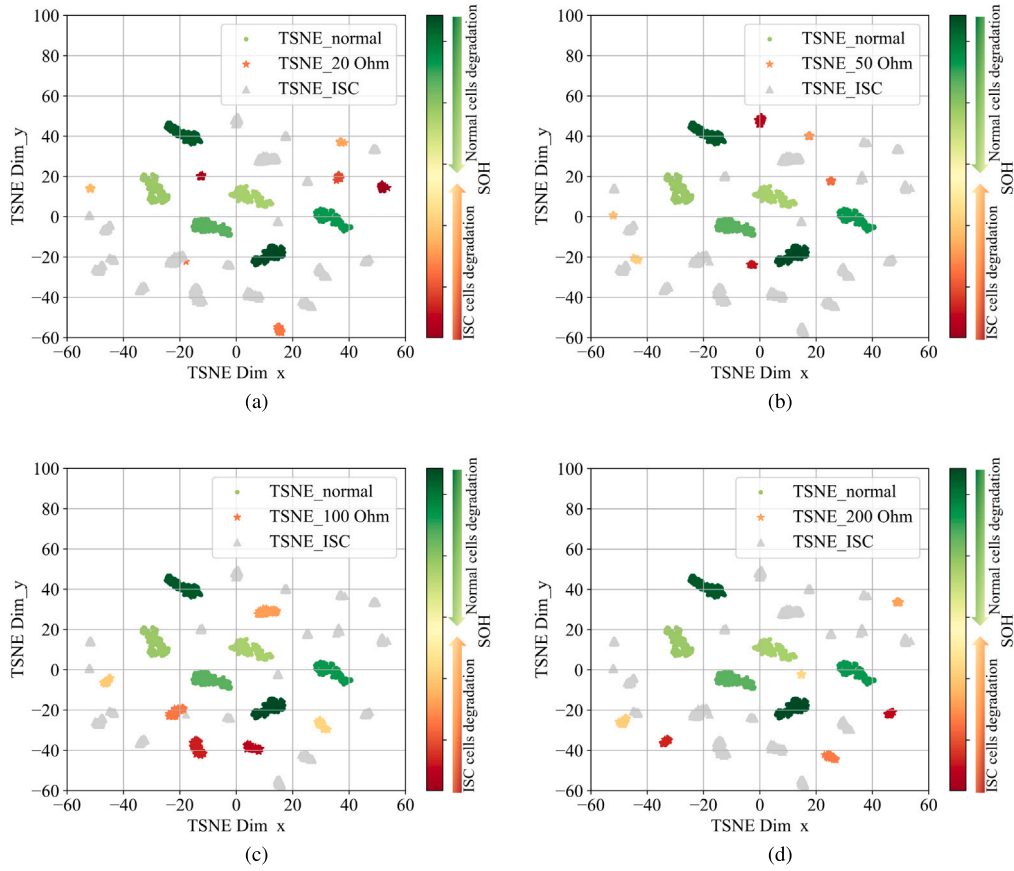


Fig. 7. Multi-label feature representation in the latent space using SPMe simulation data. (a) 20  $\Omega$  ISC; (b) 50  $\Omega$  ISC; (c) 100  $\Omega$  ISC; (d) 200  $\Omega$  ISC.

values and covariance, and  $N$  stands for the size of the fitting data. The selection of Gaussian component number is a trade-off between under- and overfitting since the minus likelihood  $-2 \cdot \log(\hat{L})$  decreases and the penalty term  $P \cdot \log(D)$  increases as the GMM complexity increases. Therefore, a low BIC indicates an optimal selection.

$$BIC = -2 \cdot \log(\hat{L}) + P \cdot \log(N) \quad (13)$$

GMM-VAEs with three, six, and nine Gaussian components are trained in the same training set. Latent features are then extracted from the common test set as the fitting data for BIC evaluation, respectively. A series of Gaussian Mixture models with 1 to 20 Gaussian components are fitted to the latent features mentioned above. The BIC scores are presented in Fig. S1. The BIC curves show a steep initial decrease and reach the minimum at five Gaussian components, indicating an optimized trade-off between fitting performance and complexity, and then increase slightly as more Gaussian components are used. The six-component GMM-VAE used in the previous sections is close to this identified optimum.

### 5.2. Kernel number evaluation in $mk$ -MMD loss

MMD loss using a mixture of Gaussian kernels with varying bandwidths in Eq. (8) is implemented instead of the single-kernel MMD to address the loss saturation, preventing gradient collapse and maintaining the sensitivity of MMD loss during training. To determine the optimal number of Gaussian kernels used in  $k$ -MMD, the MMD losses across a variety of bandwidths adapted to the covariance of total MMD loss  $\sigma$  during training process are evaluated.

As illustrated in Fig. S2, the MMD loss degrades noticeably as  $\log_2 \sigma$  deviates from  $-2$  towards either  $-10$  or  $10$ , indicating a reducing

sensitivity. Therefore, the optimal  $\log_2 \sigma$  ranges between  $-4$  and  $2$ , respectively, which corresponds to the kernel numbers between 5 and 9. The 5-kernel MMD loss used in the previous sections falls within the optimal range.

## 6. Conclusions

In this work, a fault diagnosis approach for LIB based on feature representation learning is proposed. The VAE with GMM prior distribution is trained to generate distinguishable features in latent space for normal and abnormal cells. The proposed approach is validated on the ISC simulation data with various ISC severities through SPMe model and a real battery dataset with overcharge and over-temperature abuses, presenting a prominent performance in multi-label and binary fault diagnosis.

Compared to the reconstruction residual based approach, the proposed method utilizes unsupervised learning and shows superior performance with TPR and TNR over 98% on both ISC simulation and real dataset for binary fault diagnosis. Furthermore, self-supervised learning is implemented for multi-label fault diagnosis to categorize normal cells and abnormal cells with various ISC severities. An RF classifier utilizing the latent features from the GMM-VAE encoder achieves excellent performance with TPR and TNR over 96% for normal cells and fault cells of different ISC grades, using 50% normal cell data and 15% ISC cell data.

Future work will focus on a fully unsupervised model integrating feature extraction and embedded clustering mechanism to perform both binary and multi-label diagnosis. In addition, the ISC model should consider the decrease in the equivalent ISC resistance accordingly with cell degradation that can support predicting the trigger of serious safety event, e.g. Thermal Runaway.

## CRedit authorship contribution statement

**Wenbin Li:** Writing – review & editing, Writing – original draft, Software, Methodology, Investigation, Formal analysis, Conceptualization. **Yue Yang:** Writing – review & editing, Visualization, Validation, Conceptualization. **Stefan Pischinger:** Writing – review & editing, Supervision, Resources, Project administration, Funding acquisition.

## Acknowledgments

This work was supported by the Open access funding provided by the Open Access Publishing Fund of RWTH Aachen University, financed by Deutsche Forschungsgemeinschaft (DFG, 532171154).

## Declaration of competing interest

The authors declare that they have no known competing financial interests or personal relationships that could have appeared to influence the work reported in this paper.

## Appendix A. Supplementary data

Supplementary material related to this article can be found online at <https://doi.org/10.1016/j.est.2026.120545>.

## Data availability

Data will be made available on request.

## References

- [1] S. Nyamathulla, C. Dhanamjayulu, A review of battery energy storage systems and advanced battery management system for different applications: Challenges and recommendations, *J. Energy Storage* 86 (2024) 111179, <http://dx.doi.org/10.1016/j.est.2024.111179>.
- [2] W. Liu, T. Placke, K. Chau, Overview of batteries and battery management for electric vehicles, *Energy Rep.* 8 (2022) 4058–4084, <http://dx.doi.org/10.1016/j.egy.2022.03.016>.
- [3] J. Zhao, X. Feng, M.-K. Tran, M. Fowler, M. Ouyang, A.F. Burke, Battery safety: Fault diagnosis from laboratory to real world, *J. Power Sources* 598 (2024) 234111, <http://dx.doi.org/10.1016/j.jpowsour.2024.234111>.
- [4] Y. Yao, X. Du, S. Jiang, R. Salehi, E. Huemiller, W. Shi, Prognostics of internal short circuit in lithium-ion batteries — literature survey and performance evaluation, *J. Power Sources* 648 (2025) 237203, <http://dx.doi.org/10.1016/j.jpowsour.2025.237203>.
- [5] W. Chen, X. Han, Y. Pan, Y. Yuan, X. Kong, L. Liu, Y. Sun, W. Shen, R. Xiong, Defects in lithium-ion batteries: From origins to safety risks, *Green Energy Intell. Transp.* 4 (3) (2025) 100235, <http://dx.doi.org/10.1016/j.geits.2024.100235>.
- [6] Q. Yu, C. Wang, J. Li, R. Xiong, M. Pecht, Challenges and outlook for lithium-ion battery fault diagnosis methods from the laboratory to real world applications, *eTransportation* 17 (2023) 100254, <http://dx.doi.org/10.1016/j.etrans.2023.100254>.
- [7] Q. Wang, Z. Wang, L. Zhang, P. Liu, Z. Zhang, A novel consistency evaluation method for series-connected battery systems based on real-world operation data, *IEEE Trans. Transp. Electr.* 7 (2) (2021) 437–451, <http://dx.doi.org/10.1109/TTE.2020.3018143>.
- [8] M.G. Abdolrasol, A. Ayob, M.H. Lipu, S. Ansari, T.S. Kiong, M.H. M. Saad, T.S. Ustun, A. Kalam, Advanced data-driven fault diagnosis in lithium-ion battery management systems for electric vehicles: Progress, challenges, and future perspectives, *eTransportation* 22 (2024) 100374, <http://dx.doi.org/10.1016/j.etrans.2024.100374>.
- [9] R. Xiong, W. Sun, Q. Yu, F. Sun, Research progress, challenges and prospects of fault diagnosis on battery system of electric vehicles, *Appl. Energy* 279 (2020) 115855, <http://dx.doi.org/10.1016/j.apenergy.2020.115855>.
- [10] Y. Shang, S. Wang, N. Tang, Y. Fu, K. Wang, Research progress in fault detection of battery systems: A review, *J. Energy Storage* 98 (2024) 113079, <http://dx.doi.org/10.1016/j.est.2024.113079>.
- [11] Y. Xu, X. Ge, R. Guo, W. Shen, Recent advances in model-based fault diagnosis for lithium-ion batteries: A comprehensive review, *Renew. Sustain. Energy Rev.* 207 (2025) 114922, <http://dx.doi.org/10.1016/j.rser.2024.114922>.
- [12] Z. Liu, J. Xu, Z. Zhao, Z. Zou, X. Mei, A novel battery active equalization-based internal short circuit fault diagnosis method for lithium-ion batteries, *Energy* 333 (2025) 137421, <http://dx.doi.org/10.1016/j.energy.2025.137421>.
- [13] J. Sun, S. Chen, S. Xing, Y. Guo, S. Wang, R. Wang, Y. Wu, X. Wu, A battery internal short circuit fault diagnosis method based on incremental capacity curves, *J. Power Sources* 602 (2024) 234381, <http://dx.doi.org/10.1016/j.jpowsour.2024.234381>.
- [14] J. Li, T. Li, D. Fang, Y. Wang, S. Guo, Z. Wang, Q. Yu, Internal fault diagnosis method for lithium batteries based on a failure physical model, *Eng. Fail. Anal.* 154 (2023) 107714, <http://dx.doi.org/10.1016/j.engfailanal.2023.107714>.
- [15] Q. Yu, L. Dai, R. Xiong, Z. Chen, X. Zhang, W. Shen, Current sensor fault diagnosis method based on an improved equivalent circuit battery model, *Appl. Energy* 310 (2022) 118588, <http://dx.doi.org/10.1016/j.apenergy.2022.118588>.
- [16] C. Chang, Q. Wang, J. Jiang, Y. Jiang, T. Wu, Voltage fault diagnosis of a power battery based on wavelet time-frequency diagram, *Energy* 278 (2023) 127920, <http://dx.doi.org/10.1016/j.energy.2023.127920>.
- [17] X. Zhang, J. Hong, X. Xu, Fault diagnosis of real-scenario battery systems based on modified entropy algorithms in electric vehicles, *J. Energy Storage* 63 (2023) 107079, <http://dx.doi.org/10.1016/j.est.2023.107079>.
- [18] H. Liu, L. Li, B. Duan, Y. Kang, C. Zhang, Multi-fault detection and diagnosis method for battery packs based on statistical analysis, *Energy* 293 (2024) 130465, <http://dx.doi.org/10.1016/j.energy.2024.130465>.
- [19] J. Jiang, R. Zhang, Y. Wu, C. Chang, Y. Jiang, A fault diagnosis method for electric vehicle power lithium battery based on wavelet packet decomposition, *J. Energy Storage* 56 (2022) 105909, <http://dx.doi.org/10.1016/j.est.2022.105909>.
- [20] L. Niu, J. Du, S. Li, J. Wang, C. Zhang, Y. Jiang, An online fault diagnosis method for lithium-ion batteries based on signal decomposition and dimensionless indicators selection, *J. Energy Storage* 83 (2024) 110590, <http://dx.doi.org/10.1016/j.est.2024.110590>.
- [21] L. Yao, Z. Fang, Y. Xiao, J. Hou, Z. Fu, An intelligent fault diagnosis method for lithium battery systems based on grid search support vector machine, *Energy* 214 (2021) 118866, <http://dx.doi.org/10.1016/j.energy.2020.118866>.
- [22] L. Lv, L. Zhu, S. Gao, X. Xiang, L. Wang, C. Chang, A. Tian, J. Jiang, Fault diagnosis method for lithium-ion batteries based on image features and improved isolated forests, *Energy* 338 (2025) 138849, <http://dx.doi.org/10.1016/j.energy.2025.138849>.
- [23] H. Li, G. Chen, Y. Yang, B. Shu, Z. Liu, J. Peng, Adversarial learning for robust battery thermal runaway prognostic of electric vehicles, *J. Energy Storage* 82 (2024) 110381, <http://dx.doi.org/10.1016/j.est.2023.110381>.
- [24] J. Zhang, Y. Wang, B. Jiang, H. He, S. Huang, C. Wang, Y. Zhang, X. Han, D. Guo, G. He, M. Ouyang, Realistic fault detection of li-ion battery via dynamical deep learning, *Nat. Commun.* 14 (2023) 5940, <http://dx.doi.org/10.6084/m9.figshare.23659323.v1>.
- [25] J. Guo, W. Fan, M. Amayri, N. Bouguila, Deep clustering analysis via variational autoencoder with gamma mixture latent embeddings, *Neural Netw.* 183 (2025) 106979, <http://dx.doi.org/10.1016/j.neunet.2024.106979>.
- [26] H. Peng, J. Long, C. Huang, S. Wei, Z. Ye, Multi-modal hybrid modeling strategy based on gaussian mixture variational autoencoder and spatial-temporal attention: Application to industrial process prediction, *Chemometr. Intell. Lab. Syst.* 244 (2024) 105029, <http://dx.doi.org/10.1016/j.chemolab.2023.105029>.
- [27] M. Luh, T. Blank, Comprehensive battery aging dataset: capacity and impedance fade measurements of a lithium-ion nmc/c-sio cell, *Sci. Data* 11 (2024) 1004, <http://dx.doi.org/10.1038/s41597-024-03831-x>.
- [28] V. Sulzer, S.G. Marquis, R. Timms, M. Robinson, S.J. Chapman, Python Battery Mathematical Modelling (PyBaMM), *J. Open Res. Softw.* 9 (1) (2021) 14, <http://dx.doi.org/10.5334/jors.309>.
- [29] C.-H. Chen, F. Brosa Planella, K. O'Regan, D. Gastol, W.D. Widanage, E. Kendrick, Development of experimental techniques for parameterization of multi-scale lithium-ion battery models, *J. Electrochem. Soc.* 167 (8) (2020) 080534, <http://dx.doi.org/10.1149/1945-7111/ab9050>.
- [30] L. Li, Y. Ren, K. O'Regan, U.r. Koleti, E. Kendrick, W. Widanage, J. Marco, Lithium-ion battery cathode and anode potential observer based on reduced-order electrochemical single particle model, *J. Energy Storage* 44 (2021) 103324, <http://dx.doi.org/10.1016/j.est.2021.103324>.
- [31] Z. Jia, Z. Wang, Z. Sun, X. Sun, P. Liu, F. Ruzzenenti, A multi-scenario data-driven approach for anomaly detection in electric vehicle battery systems, *eTransportation* 24 (2025) 100418, <http://dx.doi.org/10.1016/j.etrans.2025.100418>.
- [32] Z. Yang, K. Zheng, H. Zheng, F. Zhou, J. Meng, Z. Song, Multi-task learning framework for fault detection in energy storage system lithium-ion batteries: From degradation to slight overcharge, *J. Energy Storage* 127 (2025) 117164, <http://dx.doi.org/10.1016/j.est.2025.117164>.
- [33] D. Qiao, X. Wei, B. Jiang, W. Fan, H. Gong, X. Lai, Y. Zheng, H. Dai, Data-driven fault diagnosis of internal short circuit for series-connected battery packs using partial voltage curves, *IEEE Trans. Ind. Inform.* 20 (4) (2024) 6751–6761, <http://dx.doi.org/10.1109/TII.2024.3353872>.

- [34] B. Cui, H. Wang, R. Li, L. Xiang, J. Du, H. Zhao, S. Li, X. Zhao, G. Yin, X. Cheng, Y. Ma, H. Huo, P. Zuo, C. Du, Internal short circuit early detection of lithium-ion batteries from impedance spectroscopy using deep learning, *J. Power Sources* 563 (2023) 232824, <http://dx.doi.org/10.1016/j.jpowsour.2023.232824>.
- [35] D. Shen, C. Lyu, D. Yang, G. Hinds, S. Xu, M. Bai, J. Qiu, Internal short circuit diagnosis of lithium-ion battery packs considering incomplete charging under cell inconsistencies, *Appl. Energy* 401 (2025) 126797, <http://dx.doi.org/10.1016/j.apenergy.2025.126797>.